Nanoscale

PAPER

View Article Online
View Journal | View Issue

Cite this: *Nanoscale*, 2023, **15**, 15219

Heterointerface engineering of cobalt molybdenum suboxide for overall water splitting†

Renjith Nadarajan, Anju V. Gopinathan, Naduvile Purayil Dileep, Akshaya S. Sidharthan and Manikoth M. Shaijumon *

Received 26th May 2023,
Accepted 24th August 2023

DOI: 10.1039/d3nr02458j

rsc.li/nanoscale

Highly active and earth-abundant electrocatalysts for the hydrogen evolution reaction (HER) and oxygen evolution reaction (OER) are of great significance for sustainable hydrogen generation through alkaline water electrolysis. Here, with an aim to enhance the bifunctional electrocatalytic activity of cobalt molybdate towards overall water splitting, we demonstrate a simple method involving the modulation of the cobalt to molybdenum ratio and creation of phase-modulated heterointerfaces. Samples with varying Co/Mo molar ratios are obtained *via* a microwave-assisted synthesis method using appropriate starting precursors. The synthesis conditions are modified to create a heterointerface involving multiple phases of cobalt molybdenum suboxides ($CoO/CoMoO_3/Co_2Mo_3O_8$) supported on Ni foam (NF). Detailed electrochemical studies reveal that modulating the composition and hence the interface can tweak the bifunctional electrocatalytic activity of the material for HER and OER and thus improve the overall water splitting efficiency with very high durability over 500 h. To further evaluate the practical applicability of the studied catalyst in water splitting, an alkaline electrolyser is fabricated with the optimized cobalt molybdenum suboxide material (CMO-1.25) as a bifunctional electrocatalyst. A current density of 220 mA cm^{-2} @1.6 V and 670 mA cm^{-2} @1.8 V was obtained, and the device showed very good long-term durability.

1. Introduction

Current environmental conditions and growing global energy demand urge us to look for renewable, environmentally friendly, sustainable energy. In this direction, hydrogen is a promising alternative, which has immense potential as a clean and efficient fuel.[1–5] When electricity is produced from renewable energy sources, electrochemical water splitting is one of the sustainable and clean ways to produce hydrogen. The efficiency of electrochemical water splitting depends on the kinetics of the hydrogen evolution reaction (HER-cathode reaction) and oxygen evolution reaction (OER-anode reaction). Therefore, developing an efficient, durable electrocatalyst for the reactions (HER and OER) is of prime importance for enabling energy-efficient water splitting and hydrogen production.[6–8]

The platinum group of metals (PGMs) is considered the state-of-art or benchmark catalysts for HER and OER. However, low availability and high cost hamper the widespread use of PGM in commercial applications. In recent years, a variety of catalysts have been explored as efficient and potential replacement for PGM, such as transition metal chalcogenides,[9–13] phosphides,[14–17] nitrides,[18–21] carbides,[22–27] borides,[28–31] oxides,[32–34] catalyst derived from metal–organic frameworks,[35–38] covalent organic frameworks[39,40] and phthalocyanine.[41–45] Most of these materials show good durability and activity in alkaline medium, especially for OER. However, their HER kinetics in alkaline medium is remarkably inferior compared to the acidic medium. Engineering the catalyst surfaces has been shown to be an effective approach towards achieving improved activity towards both HER and OER. Such bifunctional catalyst activity for HER and OER could greatly simplify the system design and lower the cost. Creating heterostructures or hierarchical architectures of components with synergistic effects can modulate the bonding and band structure, improving the catalytic performance.[13,46–48] However, building such heterostructures with control on their phase regulation is always challenging and complex.[49,50]

Transition metal molybdates (T_MMoO_4) and their hydrates direct lot of interest as electrocatalysts because of the prominent HER activity of Mo-based materials and the flexible electronic structure between Mo and the heteroatoms (T_M = Co or Ni or Fe).[51–53] MoNi nanoparticle decorated $CoMoO_3$ cuboid arrays on NF as the scaffold ($MoNi/CoMoO_3/NF$) was shown to exhibit high stability and activity, owing to the interaction between different phases as well as the ability to increase the

School of Physics, Indian Institute of Science Education and Research Thiruvananthapuram, Maruthamala PO, Thiruvananthapuram, Kerala 695551, India. E-mail: shaiju@iisertvm.ac.in

† Electronic supplementary information (ESI) available. See DOI: https://doi.org/10.1039/d3nr02458j

active sites of $CoMoO_3$ cuboids, and the synergistic effect on the whole.[53] Bimetallic Ni nanowires and $MoNi_4/MoO_{3-x}$ nanorod arrays prepared from $NiMoO_4$ precursor by a thermal reduction method were reported to exhibit comparable HER activity to Pt/C under alkaline conditions.[53] Similarly, cobalt molybdenum suboxides ($Co_2Mo_3O_8$) and their heterostructures supported on nickel as well as cobalt foam have been studied as efficient electrocatalysts for the HER in alkaline electrolytes.[52,54–56] Recent study shows that the OER performance of CoO can be further improved by modification with MoO_2 due to the synergistic effect between MoO_2 and CoO.[57] Li *et al.* reported the 1D MoO_2-$Co_2Mo_3O_8$@C nanorods that showed favourable electrocatalytic advantages toward OER in an alkaline solution.[58]

The use of a bifunctional catalyst can make the overall system design easier and more cost-effective, and therefore, it is highly necessary to make efficient catalysts for both the HER and OER under alkaline conditions, which still remains a challenge.[7] While most of the reports on transition metal molybdate-based electrocatalysts focus on either HER or OER activity, it is to be noted that their bifunctional electrocatalytic activity (towards HER/OER) can be tuned through morphology and phase engineering approaches. Here, with an aim to enhance the bifunctional electrocatalytic activity of cobalt molybdate towards overall water splitting, we demonstrate a simple method involving the modulation of cobalt to molybdenum ratio and creation of phase-modulated heterointerfaces. Samples with varying Co/Mo molar ratios are obtained by using appropriate starting precursors, and the synthesis conditions are modified to create a different heterointerface involving multiple phases of cobalt molybdenum oxide. Detailed comparison studies reveal that modulating the composition and hence the interface can tweak the bifunctional catalytic activity of the material for electrochemical hydrogen evolution and oxygen evolution reaction and thus improve the overall water splitting efficiency.

2. Experimental

2.1 Materials

Cobalt nitrate hexahydrate ($Co(NO_3)_2{\cdot}6H_2O$, 98%), sodium molybdate (Na_2MoO_4, 98%), Pt/C (20 wt% Pt) and Nafion solution (5 wt% in alcohol) were purchased from Sigma Aldrich. Potassium hydroxide (KOH) was obtained from Alfa Aesar, and hydrochloric acid from Merck. Nickel foam (≥99%) was purchased from Incoatm and had a thickness of 1.60 mm and an area density of ~650 g m^{-2}. Deionized (DI) water was used to prepare all the aqueous solutions.

2.2 Synthesis of cobalt molybdenum oxide

Synthesis of cobalt molybdenum oxide on nickel foam (NF) was carried out using a microwave-assisted approach followed by annealing in Ar/H_2 environment. The NF was cleaned in HCl solution to remove surface oxides, followed by washing in DI water and isopropyl alcohol in sequence for 10 min each. $Co(NO_3)_2{\cdot}6H_2O$ and Na_2MoO_4 were dissolved in 20 mL of DI water (Co and Mo are in the molar ratios 1 : 1, 1.25 : 1, 1.5 : 1 and 2 : 1), stirred for 30 min, and the cleaned NF was dipped in this solution and transferred into a 30 mL microwave vial. The sealed glass vial was kept at 180 °C for 45 min and then cooled to ambient temperature. The samples were washed thoroughly with DI water and IPA and then dried at 60 °C. Further, the catalyst samples were annealed at 450 °C under an Ar/H_2 flow (100 sccm; 90 : 10) for 2 h. According to the weight change of the sample after annealing, the average loading of the catalyst on NF was determined to be nearly 0.8 mg cm^{-2}.

2.3 Synthesis of Pt/C or IrO_2 electrocatalysts on Ni foam

The Pt/C working electrodes were prepared by dispersing 4 mg Pt/C in a mixture of DI water (750 μL) and isopropyl alcohol (200 μL), followed by the addition of Nafion solution (50 μL). After sonication for 30 min, 220 μL of the Pt/C ink was slowly loaded onto a piece of cleaned NF with a geometrical surface area of 1.0 cm^2 and subsequently dried at room temperature. The loading of Pt/C is 0.8 mg cm^{-2}, equal to the loading mass of CMO on NF. A similar procedure was used to prepare commercial IrO_2 on NF, and the loading was found to be nearly 0.8 mg cm^{-2}.

2.4 Materials characterization

Powder X-ray diffraction (XRD) patterns were recorded using Empyrean, PANalytical XRD instrument with Cu Kα radiation (1.54 Å) with a step size of 0.02° in the range 10–80°. The samples' surface morphology was analyzed using a field emission scanning electron microscope (FE-SEM, Nova NanoSEM 450, FEI). Transmission electron microscopy (TEM) imaging was carried out using an electron microscope (FEI, Tecnai F30) with a 300 kV electron beam. Raman spectroscopy was performed using a 532 nm laser using a HORIBA XploraPlus Micro Raman spectrometer. High-resolution X-ray photoelectron spectroscopy (XPS) was carried out using a Scienta-Omicron with an Mg Kα source. Inductively coupled plasma optical emission spectrometry (ICP-OES) was carried out on PerkinElmer Optima 5300 DV.

2.5 Electrochemical measurements

The electrochemical measurements were performed on a Biologic SAS VMP3 electrochemical workstation in a three-electrode configuration. The as-prepared catalysts were used as working electrodes, the graphite rod and Hg/HgO electrode were used as the counter, and the reference electrodes, respectively. OER and HER measurements were carried out in 1 M KOH aqueous electrolyte. Using the Nernst equation, all the measured potentials were converted into a reversible hydrogen electrode (RHE).

$$E(vs.\ \mathrm{RHE}) = E(vs.\ \mathrm{Hg/HgO}) + E_0(\mathrm{Hg/HgO}) + 0.059 \times \mathrm{pH}$$

Potential cycling is typically done with a sweep rate of 50 mV s^{-1} before measuring the polarization curves. The polar-

ization curves were measured by linear sweep voltammetry (LSV) at a scan rate of 2 mV s^{-1} to evaluate the HER and OER performance of working electrodes. Electrochemical impedance spectroscopy (EIS) measurements were carried out in a frequency range of 100 kHz to 10 mHz with an amplitude of 5 mV. The C_{dl} value was measured using the cyclic voltammetry (CV) method, based on which the electrochemical active surface area (ECSA) of the catalysts was determined.

2.6 Electrolyser assembly

A 1.7 cm × 1.7 cm alkaline electrolyser was assembled, and oxygen and hydrogen electrocatalysts grown on NF were used as an anode and cathode, respectively. A gas diffusion layer was formed on the back side of the as-formed catalyst-loaded NF. A commercially available porous polymeric membrane (FAS 50) stable in the alkaline electrolyte is used as the separator. 1 M KOH solution was used as the electrolyte, and proper flow of electrolytes was maintained during the measurement. A temperature of 60 °C was also maintained during the entire time scale of the measurement.

3. Results and discussion

3.1 Materials characterization

Fig. 1a depicts the schematic of a two-step procedure used to fabricate the cobalt molybdenum suboxide (CMO) electrocatalyst. First, cobalt molybdenum oxide was synthesized directly on NF using a microwave-assisted synthesis method. The reaction was carried out in a microwave digester (Anton Paar Monowave 200), wherein a mixture of $Co(NO_3)_2{\cdot}6H_2O$ and Na_2MoO_4 in 15 mL of DI water was heated at 180 °C for 45 min. Samples were prepared with varying Co/Mo molar ratios of 1 : 1, 1.25 : 1, 1.5 : 1, and 2 : 1, and the formed samples are referred as CMO-1, CMO-1.25, CMO-1.5 and CMO-2, respectively. Optimized samples were grown on NF with varying geometrical area for the electrochemical measurements (Fig. 1b). Systematic studies revealed that the phase composition of the samples synthesized *via* microwave-assisted route was independent of the molar ratio of Co/Mo precursors at least in a range of 1 : 1 to 2 : 1 (Fig. S1†). However, it was found that the annealing temperature was a key factor influencing the catalytic properties.[59–61] In the present study, the as-prepared material was annealed at 450 °C for 2 h in Ar/H_2 (100 sccm), resulting in the creation of a heterointerface made of cobalt molybdenum suboxides.

The crystal structure of the samples was characterized by X-ray diffraction (XRD). The XRD results confirm the formation of the $CoMoO_4$ structure of the sample prepared *via* the microwave route (before annealing), as shown in Fig. S1† (JCPDS no. 15-0439). The XRD patterns of the annealed samples showed distinct diffraction peaks reflecting varying phase structures. XRD patterns of CMO-2 and CMO-1.5 exhibit peaks of $Co_2Mo_3O_8$ (JCPDS no. 34-0511) suboxide phase (Fig. 1c and Fig. S2†), wherein the peak at 44.2° corresponds to metallic (111) plane of Co (JCPDS no. 15-0806). The diffraction peaks of

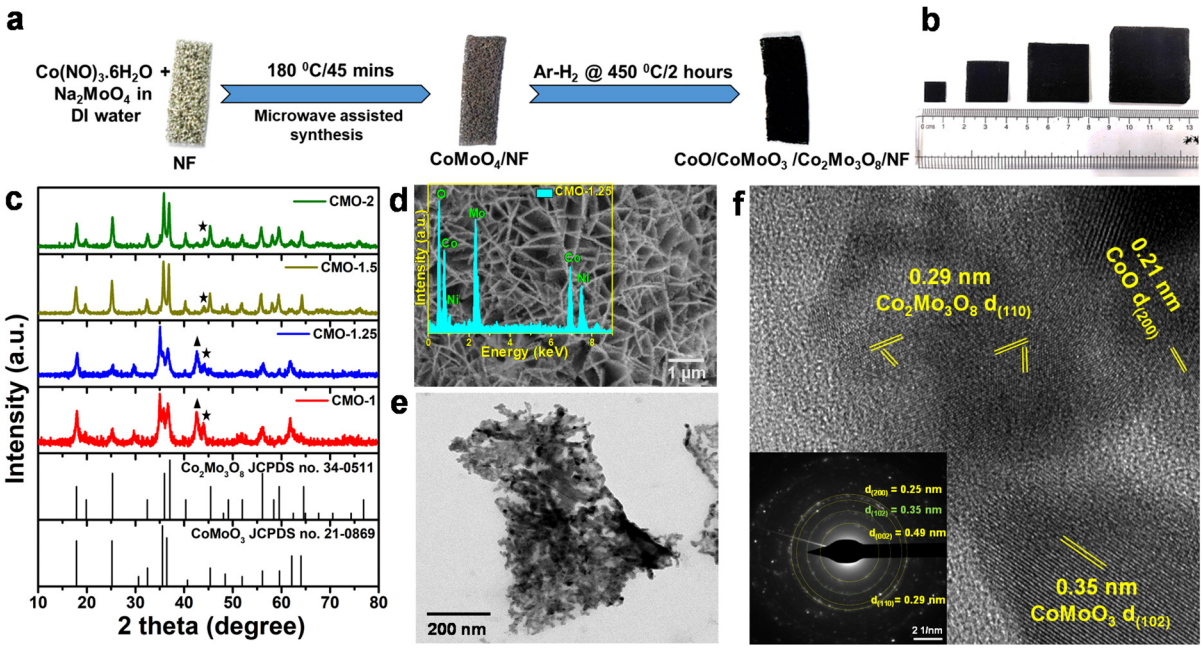

Fig. 1 (a) Schematic representation of the microwave-assisted synthesis and reduction of $CoMoO_4$ to the $CoO/CoMoO_3/Co_2Mo_3O_8$ heterointerface composite in Ar/H_2 environment (b) photograph of as-prepared CMO-1.25 catalyst grown on NF with different geometrical area (c) XRD pattern of CMO-1, CMO-1.25, CMO 1.5 and CMO-2. CMO-1 and CMO-1.25 show mixed phases of $Co_2Mo_3O_8$, $CoMoO_3$, and CoO (★ corresponds to the (111) plane of Co; ▲ corresponds to (200) plane of CoO) (d) SEM image of CMO-1.25, inset shows the EDX spectrum. (e) TEM image of CMO-1.25 (f) HR-TEM image of CMO-1.25 reveals lattice fringes with *d* spacing corresponding to $Co_2Mo_3O_8$, $CoMoO_3$, and CoO phases. Inset shows the corresponding SAED pattern.

the CMO-1 and CMO-1.25 could be indexed to a mixture of nanocrystalline $Co_2Mo_3O_8$ and $CoMoO_3$ phases along with CoO phase (Fig. S3†). The peaks observed at 36.7°, 42.6° and 61.9° correspond to CoO (JCPDS no. 01-75-0418) and the rest of peaks are attributed to the diffraction peaks of $CoMoO_3$ or $Co_2Mo_3O_8$, as marked in the plot. A detailed comparison of the XRD results of all the samples are presented in Fig. S2 and S3.†

The morphology of as-prepared sample was investigated by scanning electron microscopy (SEM). The SEM image of as-synthesized CMO-1.25 showed a well-aligned nanoplate morphology with lateral dimensions of 2 μm forming a flower-like morphology, densely covering the NF surface (Fig. 1d). The inset shows the EDX spectrum collected from the CMO-1.25, clearly revealing the presence of constituent elements. The morphology of the samples with varying compositions of Co/Mo does not seem to have changed upon annealing (Fig. S4†).

The EDX mapping images of CMO-1.25 shows an atomically uniform distribution of the Co, Mo and O after annealing (Fig. S5†). Transmission electron microscopy (TEM) images provided a thorough depiction of the sample. The sample scraped from the NF was sonicated in IPA, and a very dilute solution was drop-casted on the carbon-coated copper grids for the TEM study. A few micron-sized sheets (lateral dimension) made of closely packed nanoparticles were observed in the TEM image of CMO-1.25 (Fig. 1e).

Further analysis of the sample using high-resolution TEM (HR-TEM) and selected area electron diffraction (SAED) revealed that these sheets were composed of nanoparticles exhibiting various phases of cobalt molybdenum suboxide (Fig. 1f). While the HR-TEM image of CMO-1.25 clearly shows the presence of a heterointerface formed from cobalt molybdenum suboxide phases, $Co_2Mo_3O_8$, $CoMoO_3$, and CoO (Fig. 1f), CMO-2 was seen to exhibit $Co_2Mo_3O_8$ phase alone, as revealed from the *d* spacing of 0.249 nm and 0.354 nm that correspond to (200) and (102) planes, respectively, which is consistent with the XRD findings (Fig. S6†). Another intriguing observation from the TEM studies is that the annealed samples are highly porous, which might have resulted from the loss of oxygen atoms during the reduction process (Fig. S7†).[55] Such porous morphology favours improved ion diffusion, increases the catalytic activity towards HER and OER, and the charge transfer ability.[62]

We further performed X-ray photoelectron spectroscopy (XPS) studies to ascertain the phase and chemical state of the materials (Fig. 2 and Fig. S8†). The high resolution XPS spectra for the CMO-1.25 are shown in Fig. 2. All the spectra were calibrated with the binding energy of the C–C component at 284.8 eV. The XPS spectra of the as-prepared material obtained *via* microwave-assisted method show peaks corresponding to Co^{2+} and Mo^{6+}, indicating a single-phase $CoMoO_4$, which is in complete agreement with the XRD analysis. The microwave synthesized sample has cobalt in a Co^{2+} state, with peak positions at 796.0 and 780.4 eV corresponding to $2p_{1/2}$ and $2p_{3/2}$, respectively, with a peak separation of 15.6 eV (Fig. 2a). For the annealed sample, Co 2p XPS spectra show a pair of peaks

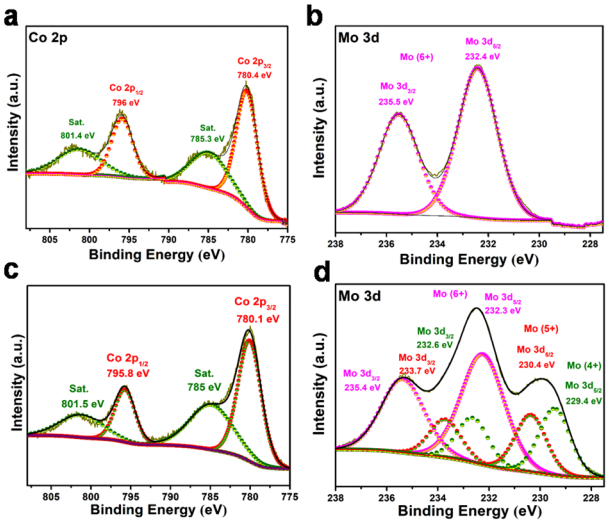

Fig. 2 XPS spectra of (a) Co 2p and (b) Mo 3d of CMO-1.25 before annealing, (c) Co 2p and (d) Mo 3d of CMO-1.25 after annealing.

corresponding to $2p_{1/2}$ and $2p_{3/2}$ with a separation of 15.7 eV and a pair of weak satellite doublet peaks (Fig. 2c). The characteristic peaks observed at binding energies of 795.8 and 780.1 eV are identified as Co^{2+} species,[63,64] whereas the other two peaks at 801.5 and 785.0 eV are the satellite peaks ascribed to the Co^{2+} ions.[65] Analysis of the Mo 3d spectrum for as-prepared CMO-1.25 shows the Mo^{6+} state corresponding to the $CoMoO_4$ phase (Fig. 2b). Interestingly, the XPS spectra recorded for the annealed CMO-1.25 exhibit mixed oxidation states for molybdenum like Mo^{4+}, Mo^{5+} and Mo^{6+} (Fig. 2d). The peaks observed at binding energies of 232.6 eV and 229.4 eV correspond to Mo^{4+}, 233.7 eV and 230.4 eV correspond to Mo^{5+}, and 235.4 eV and 232.3 eV correspond to Mo^{6+} oxidation states, which are the oxidation products of Mo species.[66,67] Further, the O 1s XPS spectra was recorded, which showed peaks at ~531.1 and ~530.1 eV, corresponding to the lattice oxygen and the bonding state of Mo–O or Co–O, respectively (Fig. S8c, g and k†).[68] The complete set of data recorded from the XPS analysis for all the studied Co/Mo composition are tabulated (Table S1, ESI†), and the corresponding high resolution spectra for all the annealed samples are shown in Fig. S8.† The inductively coupled plasma optical emission spectroscopy (ICP-OES) studies carried out for CMO-1, CMO-1.25, CMO-1.5, and CMO-2 showed a Co/Mo ratio of 0.97, 1.24, 1.65 and 1.8, respectively (Table S2†).

3.2 Electrochemical characterisation

Electrocatalytic activity of the CMO materials towards HER and OER was studied using different electrochemical methods in a 3-electrode setup. Polarization curves were recorded from the linear sweep voltammetry (LSV) studies performed in 1 M KOH solution, with Hg/HgO as the reference electrode and graphite rod as counter. All electrochemical studies have been carried out under similar conditions. Fig. 3a shows the *iR*-corrected LSVs for HER for all the studied materials, normalized with

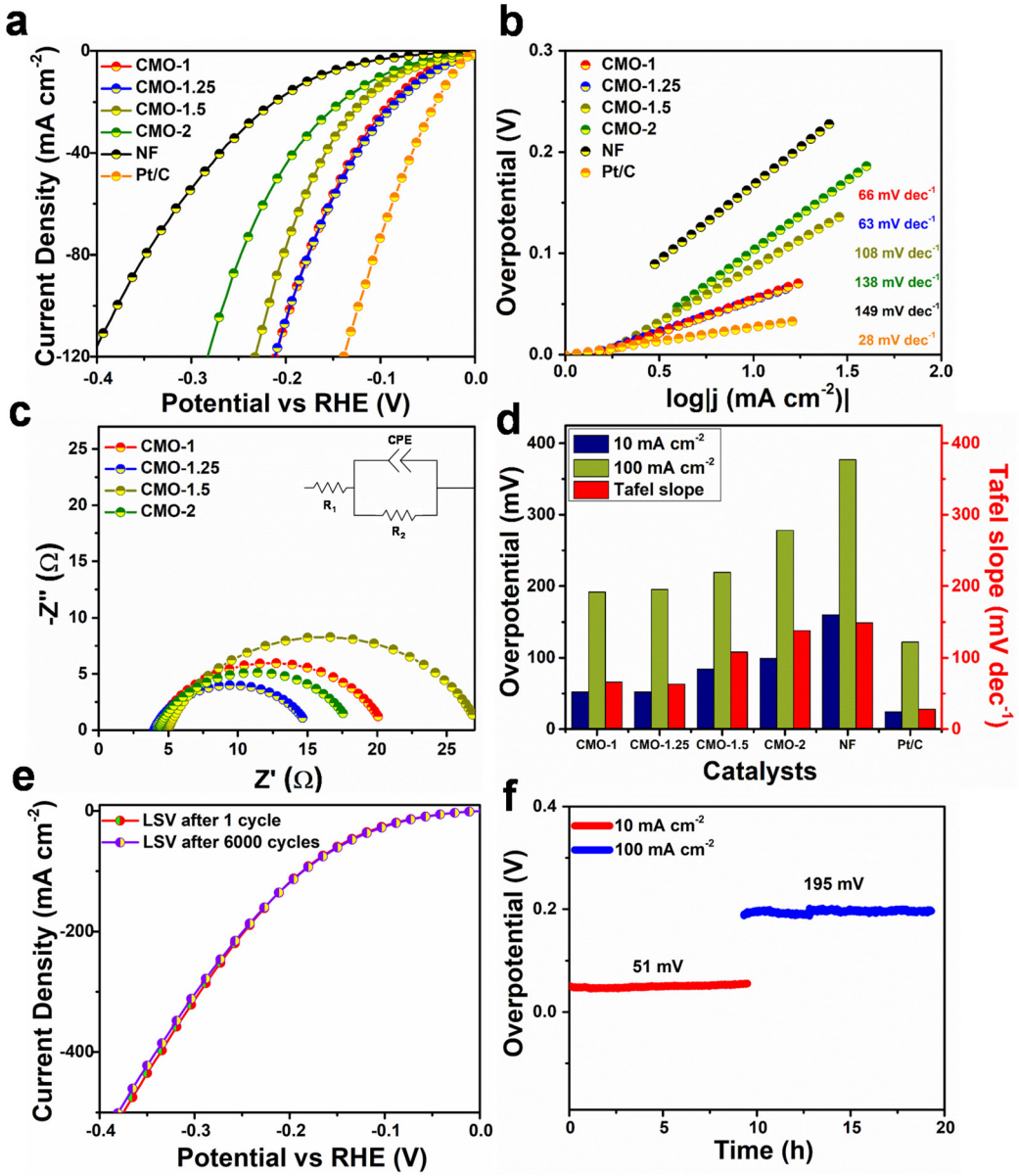

Fig. 3 (a) Polarization curves and (b) Tafel plots for HER obtained from the various catalysts studied along with control systems (c) Nyquist plots of CMO electrodes recorded at an overpotential of 30 mV in 1 M KOH, inset shows the corresponding equivalent circuit. (d) Bar diagram showing the overpotential of various CMO electrodes corresponding to current densities of 10 mA cm^{-2} and 100 mA cm^{-2}, along with the respective Tafel slopes. (e) polarization curves of CMO-1.25 for first and after 6000 cyclic voltammetry cycles, performed at a scan rate of 100 mV s^{-1} (f) Chronopotentiometry curves of CMO-1.25 at different current densities recorded for 20 h in 1 M KOH.

the geometric area of the electrode. Co/Mo molar ratio of CMO materials is seen to have a critical role in their electrocatalytic activity. CMO-1.25 exhibited significantly enhanced HER activity, compared to the other electrodes, with a low overpotential of 51 mV and 195 mV at current densities of 10 mA cm^{-2} and 100 mA cm^{-2}, respectively, for the alkaline HER. The HER LSV curves recorded for NF and Pt/C on NF are also presented for comparison. The observed values for CMO-1.25 are better than the reported studies for similar Co–Mo-based electrocatalysts towards alkaline HER.[52,69]

To gain insights into the reaction kinetics and investigate the influence of the overpotential on the steady-state current densities, corresponding Tafel plots were obtained from the respective LSVs (Fig. 3b). Tafel slopes and the exchange current densities are calculated from the Tafel equation ($\eta = a + b \log j$) by plotting the overpotential (η) as a function of $\log |j|$.[70] The smaller Tafel slope implies faster electron-transfer kinetics. The obtained Tafel slope of 63 mV dec^{-1} for the CMO-1.25 further confirms the excellent HER activity of the catalyst, compared with the other CMO catalysts with different Co/Mo molar concentrations. The overall electrocatalytic activity of CMO-1.25 is among the top level of reported non-precious alkaline HER catalysts (Fig. S9†). From the measured Tafel slope, the alkaline HER over the CMO-1.25 is believed to

follow the Volmer–Tafel mechanism, and the Tafel step is the rate-determining step.[59] We further measured the charge transfer resistance (R_{ct}) of the catalysts using electrochemical impedance spectroscopy (EIS) technique and evaluated their electrochemical surface area using the CV method.

The uncompensated ionic and ohmic resistance of the electrochemical measurement system and the R_{ct} of a catalyst are obtained from the EIS Nyquist plots.[71] R_{ct} is related to the interface charge-transfer process of an electrode, and a smaller R_{ct} value suggests a faster reaction rate, improved conductivity, which can drastically enhance the performance of the catalyst in the HER. As shown in Fig. 3c, CMO-1.25 was shown to exhibit an R_{ct} of 11.2 Ω, which was lower than that of the other CMO samples (16.6 Ω, 22.6 Ω and 14.1 Ω for CMO-1, CMO-1.5 and CMO-2 respectively). The EIS data corroborate with the results obtained from the LSV curves and the Tafel slopes, confirming the superior electrocatalytic activity of CMO-1.25. Fig. 3d compares the overpotential and Tafel slope for the studied samples. We measured the double-layer capacitance (C_{dl}) in a non-faradaic potential region to assess the electrochemical active surface area of the catalysts. Fig. S10† compares the double-layer capacitances to indicate the change in ECSA for different samples at different scan rates of 10 mV s^{-1} to 100 mV s^{-1} in 1 M KOH solution. The ECSA of the catalysts is a critical parameter in evaluating their catalytic activity since a higher ECSA usually means more exposed active sites. C_{dl}, which is calculated from CV method, is proportional to the ECSA of the catalysts. The C_{dl} for CMO-1.25 catalysts is calculated to be ~30 mF cm^{-2} while CMO-1 has 22.7 mF cm^{-2}, CMO-1.5 has 20.9 mF cm^{-2} and CMO-2 has 22.1 mF cm^{-2}. The phase-regulated growth of $CoO/CoMoO_3/Co_2Mo_3O_8$ nanoflakes could have resulted in the higher ECSA for the CMO-1.25 catalyst. The formation of defective structure of $Co_2Mo_3O_8$ resulting from the *in situ* partial reduction of $CoMoO_4$, as well as the presence of oxygen vacancies, is also believed to have contributed to higher ECSA.[55] Fig. S11a† shows the LSV curves for HER, which are normalised by ECSA. The reductive annealing of $CoMoO_4$ in an Ar/H_2 atmosphere, seems to have changed the valence state of Mo. Meanwhile, the coordination of electrons in the chemical bonds of Co–Mo–O was changed, and the resulting oxygen vacancy rate was increased, as shown in the XPS results. It is to be noted that the oxygen vacancy plays a significant role in increasing the conductivity, electrochemically active sites and surface reactivity of the catalyst.[72] Hence, the enhanced HER activity obtained for the CMO-1.25 sample would have resulted from the high oxygen vacancy ratio and its phase regulated interface with $CoO/CoMoO_3/Co_2Mo_3O_8$ hetero-structure phases.

The stability of the CMO-1.25 sample was further tested using chronopotentiometry and cyclic voltammetry (CV) methods, and the HER activity of the catalyst showed no significant change in its performance even after long cycling (6000 cycles) measurements (Fig. 3e). The catalyst exhibited a slight overpotential fluctuation of ±1 mV at a cathodic current density of 10 mA cm^{-2} over 10 h and an overpotential increase of only ±3 mV in the following 10 h of constant-current measurement performed at 100 mA cm^{-2} (Fig. 3f).

To explore the suitability of the studied catalysts for overall water splitting process, the OER activity of CMO-1, CMO-1.25, CMO-1.5 and CMO-2 catalysts grown on NF are investigated, and the corresponding polarization curves are shown in Fig. 4a. It can be seen that CMO-1.25 exhibits a much lower overpotential than other CMO catalysts. Further, the Tafel slope of CMO-1.25 is much lower (69 mV dec^{-1}), suggesting its favourable OER kinetics (Fig. 4b). The electrocatalytic OER activity of CMO-1.25 with heterointerfaces is comparable to several of the previously reported Co–Mo compounds (Fig. S12†). EIS analysis was conducted to reveal more electrode kinetics information of the catalysts. The Nyquist plots in Fig. 4c shows that the R_{ct} of CMO-1.25 catalyst is lower than the other CMO catalysts (R_{ct} values, 25.8 Ω, 19.4 Ω, 24.9 Ω and 20.9 Ω are obtained for CMO-1, CMO-1.25, CMO-1.5 and CMO-2, respectively). The overpotential corresponding to 10 mA cm^{-2} and 100 mA cm^{-2} and the obtained Tafel slopes of different CMO catalysts are compared in Fig. 4d. CV method is used to calculate the C_{dl}, which are proportional to the ECSA of the catalysts (Fig. S13†). The CMO-1.25 shows a double layer capacitance of 28.4 mF cm^{-2}, which is much larger than those of CMO-1 (25.9 mF cm^{-2}), CMO-1.5 (20.8 mF cm^{-2}) and CMO-2 (22.5 mF cm^{-2}). The high C_{dl} of CMO-1.25 suggests enhanced catalytically active surface sites for the reaction. The results shown in Fig. S11b† indicate that CMO-1.25 shows much improved OER activity compared to other CMO catalysts studied, reflecting that the enhanced OER activity of the sample is attributed not only to the increased ECSA but also the improved intrinsic activity of the catalyst due to the optimised heterointerface structure. Further, we studied the durability of the catalysts for OER and was found that the OER activity of CMO-1.25 showed only a slight decay (±20 mV) over 6000 CV cycles (Fig. 4e). The constant-current tests (10 h) also showed much improved electrochemical performance of CMO-1.25 catalyst, at anodic current densities of 10 and 100 mA cm^{-2} (Fig. 4f). Even at a larger current density of 100 mA cm^{-2}, the CMO-1.25 electrode exhibited only 6 mV increase in the overpotential, retaining 98% of its initial catalytic activity after 10 h. The obtained results clearly show excellent bi-functional electrocatalytic activity of CMO-1.25 for alkaline HER and OER, suggesting their suitability as potential electrode materials for overall water splitting.

3.3 Overall water splitting studies

The overall water splitting studies were carried out in a two-electrode cell using CMO-1.25 as anode and cathode (Fig. 5a). From the LSV plot (Fig. 5b), it is clear that CMO-1.25-based electrode exhibited 1.8 V and 1.63 V to deliver a current density of 50 mA cm^{-2} and 10 mA cm^{-2}, respectively, for overall water splitting, which is comparable to several reported works (Table S3†).[73–75] Long-term stability of the catalyst is critical for their practical implementation in water electrolysers. The full cell with CMO-1.25 catalysts showed negligible increase in the overpotential to achieve a constant current density of 10 mA cm^{-2} over 500 h of continuous electrolysis (Fig. 5c). It is interesting to note that after 100 h chronopoten-

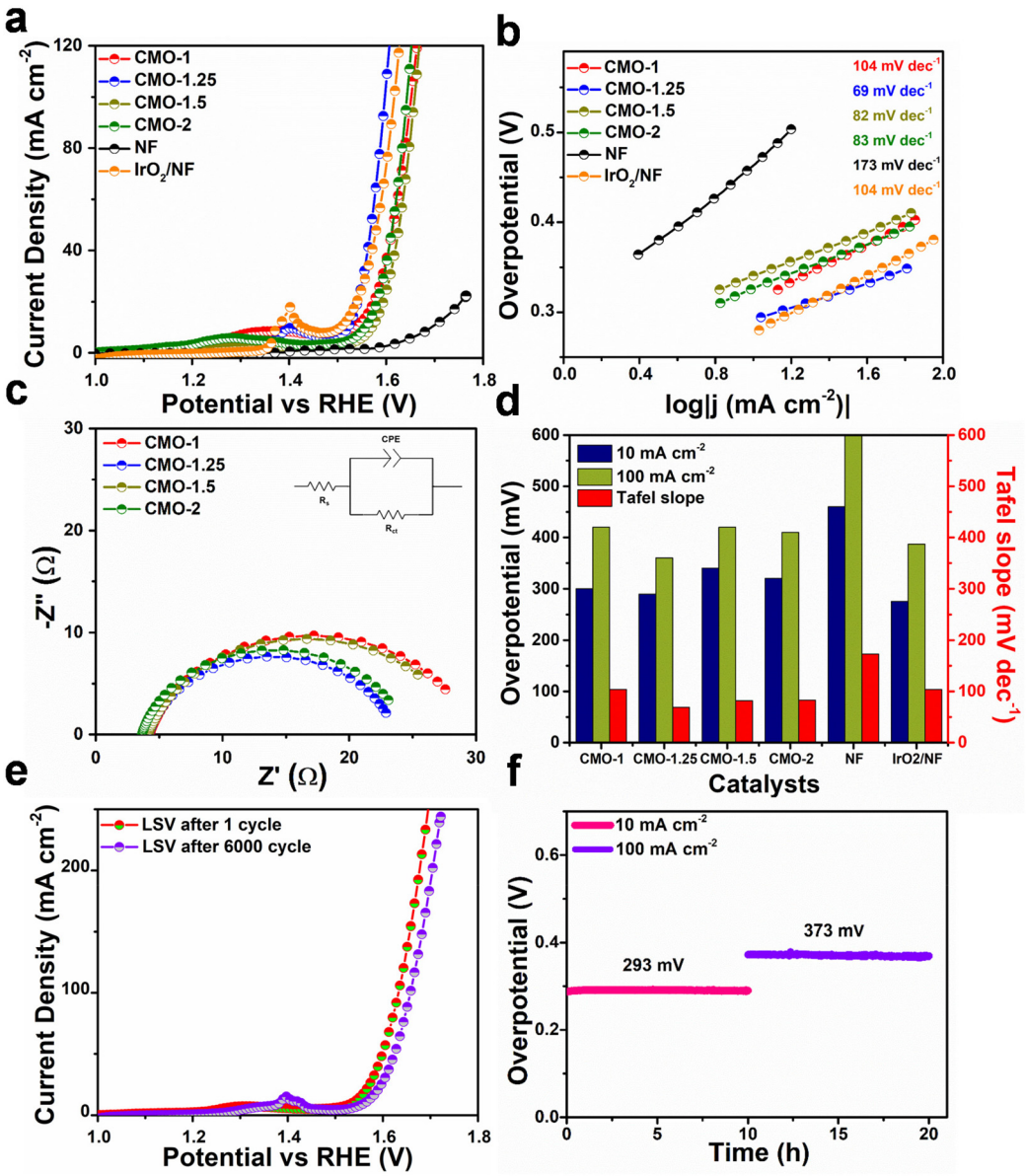

Fig. 4 (a) LSV curves for the OER activity of CMO catalysts, NF and IrO_2, studied in 1 M KOH at a scan rate of 2 mV s^{-1} (b) Tafel plots obtained from the corresponding LSV curves of the electrocatalysts. (c) Nyquist plots of CMO electrodes recorded at an overpotential of 330 mV in 1 M KOH with the corresponding equivalent circuit (inset). (d) Bar diagram comparing the overpotential of CMO catalysts for current densities of 10 mA cm^{-2} and 100 mA cm^{-2} along with corresponding Tafel slopes (e) polarization curves of CMO-1.25 for the first and after 6000 CV cycles at a scan rate of 100 mV s^{-1} (f) chronopotentiometry curves of CMO-1.25 recorded at different current densities for 20 h in 1 M KOH.

tiometry test, the CMO-1.25 was observed to retain the hierarchical structure (Fig. S14†), confirming the robust nature of the electrocatalyst for the HER and OER. We further examined the near-surface layer of the electrocatalyst after the stability test using XPS (Fig. S15†). It can be clearly seen that Co, Mo and O existed at the surface of the electrocatalyst, and the high-resolution XPS spectra were analogous to that of CMO-1.25 before the stability test, further proving the stable nature of the catalyst for the HER in alkaline media. Deconvolution of Mo 3d peaks after the stability test at HER side (Fig. S15a–c†) showed that the amount of Mo^{4+} species decreased while there was an increase in the amount of Mo^{5+} species. This could have resulted from the slight oxidation of CMO-1.25 after the prolonged stability test in highly alkaline media.[76] In addition, the deconvoluted O 1s spectrum after the stability test exhibited an increased content of –OH species which could be due to the adsorbed hydroxides and water. This result confirmed the easy adsorption of H_2O molecules in the Volmer step as described earlier. The SEM images of CMO-1.25 electrode after OER is given in Fig. S14d–f,† which also shows the retention of its pristine morphology. Deconvolution of Mo 3d peaks after the stability test at the

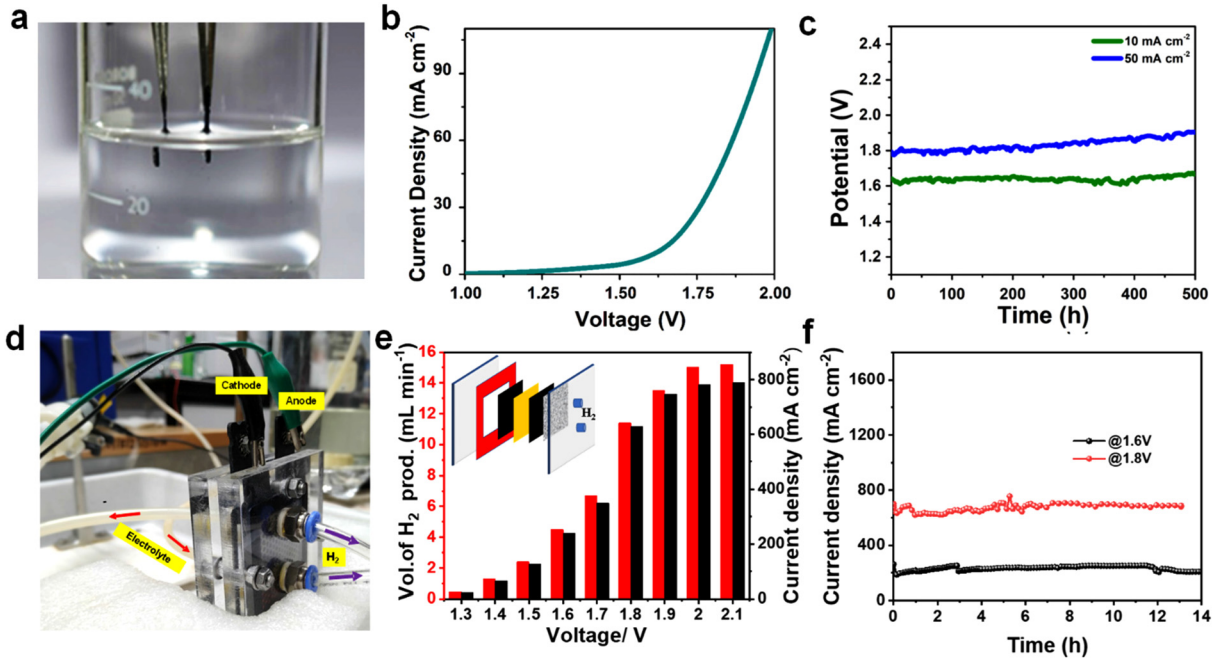

Fig. 5 (a) Photograph of the two-electrode setup employed for overall water splitting studies (b) the LSV curve obtained from two-electrode overall water splitting cell (c) chronopotentiometry curve obtained at 10 and 50 mA cm^{-2} for 500 h, showing the stability of the electrode (d) photograph of the AEM electrolyser assembly (e) volume of hydrogen produced from the water electrolyser assembly using CMO-1.25 catalyst as both anode and cathode, at different potentials. The inset shows the schematic of the AEM electrolyser setup (f) durability test recorded at 1.6 and 1.8 V for the as-assembled electrolyser.

OER side (Fig. S15d–f†) showed the presence of 4+, 5+ and 6+ oxidation states of Mo 3d. However, compared to the Mo 3d peak of the pristine CMO-1.25 catalyst provided in Fig. 2d, all the peaks are shifted towards the higher energy side and the percentage of Mo^{4+} is found to be decreased, while the percentage of Mo^{5+} and Mo^{6+} is increased, which could be attributed to the oxidation happening at the OER side.[77] All of the above results confirm that the CMO-1.25 catalyst could be used as a promising bifunctional candidate in water splitting reaction.

We also fabricated an anion exchange membrane electrolyser using the bifunctional CMO-1.25 catalyst to evaluate its practical applicability in overall water splitting (Fig. 5d). The schematic of the electrolyser setup is shown as inset of Fig. 5e. The reactor consists of an anion exchange membrane (Fumasep, FAS 50) at the middle, two gaskets on its sides, and with two 1.7 × 1.7 cm electrodes (using CMO-1.25 electrocatalyst) for HER and OER. Two polar plates are connected at the end. The FAS membrane was activated in 1 M KOH for 24 h before the experiment and used as such for the experiments. Throughout the experiment, a constant electrolyte flow (1 M KOH) was maintained in the reactor at 60 °C. The potentiodynamic polarization curve recorded for the electrolyser with CMO-1.25 as HER and OER electrocatalysts are shown in Fig. S16a† and Fig. 5e. The experiment is done by holding at a different potential, from 1.3 V to 2.1 V, for 60 s. The obtained polarization curves show that at 1.5 V the cell delivers a current density of 126 mA cm^{-2}.

The cell shows a very low current density at 1.3 V (23 mA cm^{-2}), and the current obtained from the electrolyser increased exponentially with voltage and reached to almost constant value after 2 V (781 mA cm^{-2}). The current findings are superior to several of the similar reported studies.[60,74,75,78–81]

As compared to industrial alkaline water electrolyser, which require 1.7 to 2.4 V to reach 300 mA cm^{-2} at 60–90 °C, the present cell delivers a current density of 350 mA cm^{-2} at 1.7 V. This clearly shows the high energy efficiency of the reactor with CMO-1.25 bifunctional electrocatalysts for overall water splitting.[82] The performance of the fabricated electrolyser reactor is compared with the previously reported studies (Table S4†). The amount of hydrogen generated at different voltages was measured using an inverted burette (displacement method), and the obtained values are given in Fig. 5e and Fig. S16b.† As shown in Fig. S16b,† the calculated amount of hydrogen generated by the displacement method (experimentally) is in correlation with the calculated values using Columbic method (theoretical), except that there is a slight variation in the high current density region. Moreover, the amount of hydrogen generated at 1.8 V is measured to be ~ 11–12 mL min^{-1}, *i.e.*, with 85–95% coulombic efficiency. The long-term stability of the device was studied at constant operating potentials of 1.6 V and 1.8 V (Fig. 5f). The cell gives a current density of 220 mA cm^{-2} @1.6 V and 670 mA cm^{-2} @1.8 V. The device showed very good long-term durability and retains a stable performance with 95% of its activity at 1.6 V and 1.8 V over 12 h. The present work clearly shows that the CMO-1.25 electrocatalyst exhibits excellent stability and activity for overall water splitting and has full potential for industrial

implementation towards large scale hydrogen production. The impressive bifunctional electrocatalytic activity of the material is resulted from the synergistic effect of the heterointerface formed by the cobalt molybdenum suboxides.

4. Conclusion

In summary, we demonstrated a simple approach to tune the electrocatalytic bifunctional activity of cobalt molybdate-based electrocatalyst by optimizing the cobalt to molybdenum ratio, thus creating phase-modulated heterointerfaces involving multiple phases of cobalt molybdenum suboxides (CoO/$CoMoO_3$/$Co_2Mo_3O_8$) supported on NF. The optimized catalyst (CMO-1.25) showed good OER and HER activity in 1 M KOH solution, with an OER overpotential of 290 mV @10 mA cm^{-2}, a Tafel slope of 69 mV dec^{-1} and HER overpotential of 52 mV @10 mA cm^{-2}, with a Tafel slope of 63 mV dec^{-1}. An alkaline electrolyser was further fabricated to evaluate the practical applicability of the studied catalyst in water splitting, using the studied material (CMO-1.25) as bifunctional electrocatalyst. A current density of 220 mA cm^{-2} @1.6 V and 670 mA cm^{-2} @1.8 V was obtained, with very good long-term durability, clearly indicating good promise for alkaline water electrolysis.

Author contributions

RN and MMS conceived the idea and designed the experiments. RN performed materials synthesis and electrochemical measurements. RN and AVG performed the overall water splitting studies and data analysis. RN, AVG, NPD, and AS performed the data analysis. RN, AVG and MMS wrote the manuscript with inputs from NPD and AS. MMS supervised the work.

Conflicts of interest

The authors declare no competing financial interest.

Acknowledgements

M. M. S. acknowledges the Department of Science & Technology, Govt. of India (DST/TMD/HFC/2k18/136), Science and Engineering Research Board, Department of Science and Technology, India (CRG/2021/006246), and IISER Thiruvananthapuram for the financial support. R. N. is grateful to the University Grants Commission (UGC), Govt. of India, for the Ph.D. scholarship. N. P. D. is grateful to CSIR, Govt. of India, for the financial assistance.

References

1 M. S. Dresselhaus and I. L. Thomas, *Nature*, 2001, **414**, 332–337.
2 J. K. Norskov and C. H. Christensen, *Science*, 2006, **312**, 1322–1323.
3 J. A. Turner, *Science*, 2004, **305**, 972–974.
4 Y. Ding, K.-W. Cao, J.-W. He, F.-M. Li, H. Huang, P. Chen and Y. Chen, *Chin. J. Catal.*, 2022, **43**, 1535–1543.
5 Q. Xue, X.-Y. Bai, Y. Zhao, Y.-N. Li, T.-J. Wang, H.-Y. Sun, F.-M. Li, P. Chen, P. Jin, S.-B. Yin and Y. Chen, *J. Energy Chem.*, 2022, **65**, 94–102.
6 Y. Zhang and L. Qi, *Nanoscale*, 2022, **14**, 12196–12218.
7 D. T. Dung, D. Van Lam, E. Roh, S. Ji, J. M. Yuk, J.-H. Kim, H. Kim and S.-M. Lee, *Nanoscale*, 2023, **15**, 1794–1805.
8 Z. Wang, J. Li, S. Liu, G. Shao and X. Zhao, *Nanoscale*, 2022, **14**, 16944–16951.
9 P. V. Sarma, T. V. Vineesh, R. Kumar, V. Sreepal, R. Prasannachandran, A. K. Singh and M. M. Shaijumon, *ACS Catal.*, 2020, **10**, 6753–6762.
10 M. Razavi, M. Sookhakian, B. T. Goh, H. Bahron, E. Mahmoud and Y. Alias, *Nanoscale Res. Lett.*, 2022, **17**, 9.
11 Y. Yan, B. Xia, Z. Xu and X. Wang, *ACS Catal.*, 2014, **4**, 1693–1705.
12 J. Benson, M. Li, S. Wang, P. Wang and P. Papakonstantinou, *ACS Appl. Mater. Interfaces*, 2015, **7**, 14113–14122.
13 N. P. Dileep, P. V. Sarma, R. Prasannachandran, V. Surendran and M. M. Shaijumon, *ACS Appl. Nano Mater.*, 2021, **4**, 7206–7212.
14 B. Liu, B. Cao, Y. Cheng, P. Jing, J. Zhao, R. Gao, A. O'Mullane, H. Zhu, K. Liu, X. Sun, Y. Du and J. Zhang, *iScience*, 2020, **23**, 101264.
15 P. Xiao, W. Chen and X. Wang, *Adv. Energy Mater.*, 2015, **5**, 1–13.
16 T. Liu, D. Liu, F. Qu, D. Wang, L. Zhang, R. Ge, S. Hao, Y. Ma, G. Du, A. M. Asiri, L. Chen and X. Sun, *Adv. Energy Mater.*, 2017, **7**, 1700020.
17 P. Zhou, D. Liu, Z. Wen, M. Chen, Q. Liu, Y. Ke, S. Li, S. Chen, C. T. Kwok, S. Wang, Y. Tang and H. Pan, *Int. J. Hydrogen Energy*, 2021, **46**, 18878–18886.
18 L. Lin, S. Piao, Y. Choi, L. Lyu, H. Hong, D. Kim, J. Lee, W. Zhang and Y. Piao, *EnergyChem*, 2022, **4**, 100072.
19 Y. Abghoui and E. Skúlason, *J. Phys. Chem. C*, 2017, **121**, 24036–24045.
20 W. F. Chen, K. Sasaki, C. Ma, A. I. Frenkel, N. Marinkovic, J. T. Muckerman, Y. Zhu and R. R. Adzic, *Angew. Chem., Int. Ed.*, 2012, **51**, 6131–6135.
21 D. Ologunagba and S. Kattel, *Phys. Chem. Chem. Phys.*, 2022, **24**, 12149–12157.
22 S. K. Kim, Y. Qiu, Y. J. Zhang, R. Hurt and A. Peterson, *Appl. Catal., B*, 2018, **235**, 36–44.
23 D. V. Esposito, S. T. Hunt, Y. C. Kimmel and J. G. Chen, *J. Am. Chem. Soc.*, 2012, **134**, 3025–3033.
24 M. Kuang, W. Huang, C. Hegde, W. Fang, X. Tan, C. Liu, J. Ma and Q. Yan, *Mater. Horiz.*, 2020, **7**, 32–53.

25 S. Meyer, A. V. Nikiforov, I. M. Petrushina, K. Köhler, E. Christensen, J. O. Jensen and N. J. Bjerrum, *Int. J. Hydrogen Energy*, 2015, **40**, 2905–2911.
26 H. Zhang, X. Yang, H. Zhang, J. Ma, Z. Huang, J. Li and Y. Wang, *Chem. – Eur. J.*, 2021, **27**, 5074–5090.
27 C. Tang, A. Sun, Y. Xu, Z. Wu and D. Wang, *J. Power Sources*, 2015, **296**, 18–22.
28 Y. Jiang and Y. Lu, *Nanoscale*, 2020, **12**, 9327–9351.
29 D. Wang, Y. Song, H. Zhang, X. Yan and J. Guo, *J. Electroanal. Chem.*, 2020, **861**, 113953.
30 N. Wang, A. Xu, P. Ou, S. F. Hung, A. Ozden, Y. R. Lu, J. Abed, Z. Wang, Y. Yan, M. J. Sun, Y. Xia, M. Han, J. Han, K. Yao, F. Y. Wu, P. H. Chen, A. Vomiero, A. Seifitokaldani, X. Sun, D. Sinton, Y. Liu, E. H. Sargent and H. Liang, *Nat. Commun.*, 2021, **12**, 2–10.
31 S. Wang, M. Khazaei, J. Wang and H. Hosono, *J. Mater. Chem. C*, 2021, **9**, 9212–9221.
32 E. C. Lovell, X. Lu, Q. Zhang, J. Scott and R. Amal, *Chem. Commun.*, 2020, **56**, 1709–1712.
33 L. Zhang, Q. Fan, K. Li, S. Zhang and X. Ma, *Sustainable Energy Fuels*, 2020, **4**, 5417–5432.
34 A. Y. Faid, A. O. Barnett, F. Seland and S. Sunde, *Electrochim. Acta*, 2020, **361**, 137040.
35 J. Du, F. Li and L. Sun, *Chem. Soc. Rev.*, 2021, **50**, 2663–2695.
36 W. Zheng and L. Y. S. Lee, *ACS Energy Lett.*, 2021, **6**, 2838–2843.
37 H. Liu, J. Guan, S. Yang, Y. Yu, R. Shao, Z. Zhang, M. Dou, F. Wang and Q. Xu, *Adv. Mater.*, 2020, **32**, 1–8.
38 C.-P. Wang, Y. Feng, H. Sun, Y. Wang, J. Yin, Z. Yao, X.-H. Bu and J. Zhu, *ACS Catal.*, 2021, **11**, 7132–7143.
39 C. Y. Lin, D. Zhang, Z. Zhao and Z. Xia, *Adv. Mater.*, 2018, **30**, 1–16.
40 X. Zhao, P. Pachfule and A. Thomas, *Chem. Soc. Rev.*, 2021, **50**, 6871–6913.
41 A. Abbaspour and E. Mirahmadi, *Electrochim. Acta*, 2013, **105**, 92–98.
42 K. Prabhu CP, S. Aralekallu, V. A. Sajjan, M. Palanna, S. Kumar and L. K. Sannegowda, *Sustainable Energy Fuels*, 2021, **5**, 1448–1457.
43 A. Koca, *Electrochem. Commun.*, 2009, **11**, 838–841.
44 S. Yang, Y. Yu, X. Gao, Z. Zhang and F. Wang, *Chem. Soc. Rev.*, 2021, **50**, 12985–13011.
45 L. Chen, R. U. R. Sagar, J. Chen, J. Liu, S. Aslam, F. Nosheen, T. Anwar, N. Hussain, X. Hou and T. Liang, *Int. J. Hydrogen Energy*, 2021, **46**, 19338–19346.
46 D. Zheng, L. Yu, W. Liu, X. Dai, X. Niu, W. Fu, W. Shi, F. Wu and X. Cao, *Cell Rep. Phys. Sci.*, 2021, **2**, 100443.
47 Q. Xue, X.-Y. Bai, Y. Zhao, Y.-N. Li, T.-J. Wang, H.-Y. Sun, F.-M. Li, P. Chen, P. Jin, S.-B. Yin and Y. Chen, *J. Energy Chem.*, 2022, **65**, 94–102.
48 R. Prasannachandran, T. V. Vineesh, M. B. Lithin, R. Nandakishore and M. M. Shaijumon, *Chem. Commun.*, 2020, **56**, 8623–8626.
49 A. Wu, Y. Xie, H. Ma, C. Tian, Y. Gu, H. Yan, X. Zhang, G. Yang and H. Fu, *Nano Energy*, 2018, **44**, 353–363.
50 Z. Li, M. Hu, P. Wang, J. Liu, J. Yao and C. Li, *Coord. Chem. Rev.*, 2021, **439**, 213953.
51 S. Zhao, J. Huang, Y. Liu, J. Shen, H. Wang, X. Yang, Y. Zhu and C. Li, *J. Mater. Chem. A*, 2017, **5**, 4207–4214.
52 Y. Ou, W. Tian, L. Liu, Y. Zhang and P. Xiao, *J. Mater. Chem. A*, 2018, **6**, 5217–5228.
53 D. Wang, C. Han, Z. Xing, Q. Li and X. Yang, *J. Mater. Chem. A*, 2018, **6**, 15558–15563.
54 T. Ouyang, X. T. Wang, X. Q. Mai, A. N. Chen, Z. Y. Tang and Z. Q. Liu, *Angew. Chem., Int. Ed.*, 2020, **59**, 11948–11957.
55 M. Zang, N. Xu, G. Cao, Z. Chen, J. Cui, L. Gan, H. Dai, X. Yang and P. Wang, *ACS Catal.*, 2018, **8**, 5062–5069.
56 Z. Liu, C. Zhan, L. Peng, Y. Cao, Y. Chen, S. Ding, C. Xiao, X. Lai, J. Li, S. Wei, J. Wang and J. Tu, *J. Mater. Chem. A*, 2019, **7**, 16761–16769.
57 B. B. Li, Y. Q. Liang, X. J. Yang, Z. D. Cui, S. Z. Qiao, S. L. Zhu, Z. Y. Li and K. Yin, *Nanoscale*, 2015, **7**, 16704–16714.
58 Y. Li, H. Xu, H. Huang, C. Wang, L. Gao and T. Ma, *Chem. Commun.*, 2018, **54**, 2739–2742.
59 W. Hu, Q. Shi, Z. Chen, H. Yin, H. Zhong and P. Wang, *ACS Appl. Mater. Interfaces*, 2021, **13**, 8337–8343.
60 B. Lin, J. Chen, R. Yang, S. Mao, M. Qin and Y. Wang, *Appl. Catal., B*, 2022, **316**, 121666.
61 J. A. Rodriguez, J. Y. Kim, J. C. Hanson and J. L. Brito, *Catal. Lett.*, 2002, **82**, 103–109.
62 Y. Zhang, H. Mei, J. Yang, S. Wang, H. Gao, X. Jia, J. Yan, Y. Cao, H. Luo and K. Gao, *Ionics*, 2020, **26**, 3579–3590.
63 L. Xu, Q. Jiang, Z. Xiao, X. Li, J. Huo, S. Wang and L. Dai, *Angew. Chem.*, 2016, **128**, 5363–5367.
64 L. Zhuang, L. Ge, Y. Yang, M. Li, Y. Jia, X. Yao and Z. Zhu, *Adv. Mater.*, 2017, **29**, 1606793.
65 L. Soriano, M. Abbate, A. Fernández, A. R. González-Elipe, F. Sirotti and J. M. Sanz, *J. Phys. Chem. B*, 1999, **103**, 6676–6679.
66 D. Zheng, P. Cheng, Q. Yao, Y. Fang, M. Yang, L. Zhu and L. Zhang, *J. Alloys Compd.*, 2020, **848**, 156588.
67 L. Zhang, T. Wang, L. Sun, Y. Sun, T. Hu, K. Xu and F. Ma, *J. Mater. Chem. A*, 2017, **5**, 19752–19759.
68 L. Zhang, Y. Song, W. Wu, R. Bradley, Y. Hu, Y. Liu and S. Guo, *Front. Chem. Sci. Eng.*, 2021, **15**, 156–163.
69 Z. Liu, C. Zhan, L. Peng, Y. Cao, Y. Chen, S. Ding, C. Xiao, X. Lai, J. Li, S. Wei, J. Wang and J. Tu, *J. Mater. Chem. A*, 2019, **7**, 16761–16769.
70 J. Zhu, L. Hu, P. Zhao, L. Y. S. Lee and K.-Y. Wong, *Chem. Rev.*, 2020, **120**, 851–918.
71 D. Lin and A. Lasia, *J. Electroanal. Chem.*, 2017, **785**, 190–195.
72 L. Li, J. Zhang, J. Lei, J. Xu, B. Shang, L. Liu, N. Li and F. Pan, *J. Mater. Chem. A*, 2018, **6**, 7099–7106.
73 B. Zhang, G. Liu, X. Yao, X. Li, B. Jin, L. Zhao, X. Lang, Y. Zhu and Q. Jiang, *ACS Appl. Nano Mater.*, 2021, **4**, 5383–5393.
74 D. Liu, Q. Lu, Y. Luo, X. Sun and A. M. Asiri, *Nanoscale*, 2015, **7**, 15122–15126.

75 X. Xiao, D. Huang, Y. Fu, M. Wen, X. Jiang, X. Lv, M. Li, L. Gao, S. Liu, M. Wang, C. Zhao and Y. Shen, *ACS Appl. Mater. Interfaces*, 2018, **10**, 4689–4696.
76 Y. Ou, W. Tian, L. Liu, Y. Zhang and P. Xiao, *J. Mater. Chem. A*, 2018, **6**, 5217–5228.
77 Y. Jin and P. K. Shen, *J. Mater. Chem. A*, 2015, **3**, 20080–20085.
78 J. Yu, Q. Li, Y. Li, C. Y. Xu, L. Zhen, V. P. Dravid and J. Wu, *Adv. Funct. Mater.*, 2016, **26**, 7644–7651.
79 B. Sarkar, D. Das and K. K. Nanda, *Green Chem.*, 2020, **22**, 7884–7895.
80 R. Soni, S. Miyanishi, H. Kuroki and T. Yamaguchi, *ACS Appl. Energy Mater.*, 2021, **4**, 1053–1058.
81 N. Mushtaq, C. Qiao, H. Tabassum, M. Naveed, M. Tahir, Y. Zhu, M. Naeem, W. Younas and C. Cao, *Sustainable Energy Fuels*, 2020, **4**, 5294–5300.
82 T. Kou, S. Wang and Y. Li, *ACS Mater. Lett.*, 2021, **3**, 224–234.